

Tunable Spin-Polarized States in Graphene on a Ferrimagnetic Oxide Insulator

Junxiong Hu, Yulei Han, Xiao Chi, Ganesh Ji Omar,* Mohammed Mohammed Esmail Al Ezzi, Jian Gou, Xiaojiang Yu, Rusydi Andriwo, Kenji Watanabe, Takashi Taniguchi, Andrew Thye Shen Wee, Zhenhua Qiao,* and A. Ariando*

Spin-polarized two-dimensional (2D) materials with large and tunable spin-splitting energy promise the field of 2D spintronics. While graphene has been a canonical 2D material, its spin properties and tunability are limited. Here, this work demonstrates the emergence of robust spin-polarization in graphene with large and tunable spin-splitting energy of up to 132 meV at zero applied magnetic fields. The spin polarization is induced through a magnetic exchange interaction between graphene and the underlying ferrimagnetic oxide insulating layer, $\text{Tm}_3\text{Fe}_5\text{O}_{12}$, as confirmed by its X-ray magnetic circular dichroism (XMCD). The spin-splitting energies are directly measured and visualized by the shift in their Landau-fan diagram mapped by analyzing the measured Shubnikov-de-Haas (SdH) oscillations as a function of applied electric fields, showing consistent fit with the first-principles and machine learning calculations. Further, the observed spin-splitting energies can be tuned over a broad range between 98 and 166 meV by field cooling. The methods and results are applicable to other 2D (magnetic) materials and heterostructures, and offer great potential for developing next-generation spin logic and memory devices.

1. Introduction

Two-dimensional (2D) van der Waals heterostructures comprising various 2D layered materials have emerged as promising building blocks for future ultrafast and low-power electronics.^[1,2] Particularly, the integration of 2D nonmagnetic and magnetic materials enables efficient spin generation, transport, and modulation by magnetic gates, which is the basis for 2D all-spin logic circuitries.^[3–5] To create spin-logic devices, the generation of spin current and long spin transport are the prerequisites. Graphene is an ideal spin channel due to its long spin diffusion length and long spin lifetime even at room temperature.^[6,7] Although pristine graphene is not intrinsically spin-polarized, magnetic proximity effect (MPE) can be used to induce spin splitting in graphene by coupling with magnetic substrates, leading

J. Hu, X. Chi, G. J. Omar, M. M. E. Al Ezzi, J. Gou, R. Andriwo, A. T. S. Wee, A. Ariando

Department of Physics
National University of Singapore
Singapore 117542, Singapore

E-mail: ganesh@nus.edu.sg; ariando@nus.edu.sg

J. Hu, M. M. E. Al Ezzi

Centre for Advanced 2D Materials and Graphene Research Centre
National University of Singapore
Singapore 117551, Singapore

Y. Han

International Center for Quantum Design of Functional Materials
CAS Key Laboratory of Strongly-Coupled Quantum Matter Physics
and Department of Physics
University of Science and Technology of China
Hefei, Anhui 230026, China

 The ORCID identification number(s) for the author(s) of this article can be found under <https://doi.org/10.1002/adma.202305763>

© 2023 The Authors. Advanced Materials published by Wiley-VCH GmbH. This is an open access article under the terms of the Creative Commons Attribution-NonCommercial-NoDerivs License, which permits use and distribution in any medium, provided the original work is properly cited, the use is non-commercial and no modifications or adaptations are made.

DOI: 10.1002/adma.202305763

Y. Han

Department of Physics
Fuzhou University
Fuzhou, Fujian 350108, China

X. Chi, X. Yu

Singapore Synchrotron Light Source
National University of Singapore
5 Research Link, Singapore 117603, Singapore

K. Watanabe

Research Center for Functional Materials
National Institute for Materials Science
Tsukuba, Ibaraki 305-0044, Japan

T. Taniguchi

International Center for Materials Nanoarchitectonics
National Institute for Materials Science
Tsukuba, Ibaraki 305-0044, Japan

Z. Qiao

Hefei National Laboratory
University of Science and Technology of China
Hefei 230088, China

E-mail: qiao@ustc.edu.cn

to spin-dependent transport in magnetic graphene.^[8–10] The proximity-induced spin splitting energy, originating from the electron wavefunction overlap between two adjacent materials, is a result of interface exchange interaction^[11–13] and has been observed through Zeeman spin Hall effect,^[8,10] anomalous Hall effect,^[14,15] and Hanle precession measurements.^[4,9,16] However, none of these previous experiments could directly quantify spin-splitting energy. Moreover, the induced spin-splitting energy (which defines the degree of spin-polarized density of charge carriers) has been limited to only a few tens of meV (see summary in Table S1, Supporting Information).

The goal of MPE is to achieve a considerable spin-splitting energy while maintaining the exceptional capabilities of spin transport in magnetic graphene.^[1] Theoretically, spin splitting can be enhanced by reducing the separation between the graphene sheet and magnetic substrate^[11,12] or by doping metal atoms.^[17,18] However, it is challenging to achieve this experimentally despite the recent demonstration of spin-splitting enhancement in monolayer graphene by doping with Eu atoms.^[19] Previously, a field cooling technique has been used to enhance the spin-splitting energy in graphene/antiferromagnet CrSe heterostructure.^[20] The magnetic order at the interface can be modulated by the field cooling, enabling the enhancement of the spin splitting energy. However, the CrSe magnetic substrate is conducting and inevitably short-circuits the graphene layer, making it difficult to disentangle the true origin of the effects from the substrate. Therefore, spin-splitting enhanced by a field cooling begs for a further direct experimental demonstration that can be achieved by using a magnetic insulator,^[21] as demonstrated in our work.

In this article, we directly quantify spin-splitting energy in magnetic graphene using Landau-fan shifts attained from the electric-field tuning of the Shubnikov-de-Haas (SdH) oscillation frequency. By coupling with a ferrimagnetic insulator, Tm₃Fe₅O₁₂ (TmIG), we observe a strong spin splitting energy of 132 meV at 2 K. First-principles calculations reveal that TmIG induces an electron doping to graphene, and the proximity-induced spin splitting energy can be up to 133 meV, consistent with that obtained from Landau-fan shifts. Moreover, the spin splitting is visualized by the color map of the Landau-fan diagram. Furthermore, we demonstrate that the field cooling technique can be applied to our graphene/TmIG heterostructure, leading to the tuning of the spin splitting energy between 98 and 166 meV. This result is supported by our machine learning fitting based on a phenomenological model. Finally, the spin polarization of graphene π orbitals is probed directly using X-ray magnetic circular dichroism (XMCD) and is confirmed to originate from the carbon edges.

2. Results

2.1. Concept of Landau-Fan Shift

Graphene exhibits a Dirac-cone low-energy spectrum with linear energy dispersion, protected by both inversion and time-reversal symmetries, and thus the low-energy quasiparticles in graphene behave as massless Dirac fermions.^[22] Under a perpendicular magnetic field B , the resistivity of the Dirac fermion can show quantum oscillations associated with its discrete dis-

persionless Landau-levels (LLs) that can be described by a sequence function, E_N , of the square-root of field and LL-index N as $E_N = \text{sgn}(N)\sqrt{(\alpha|N|B)}$, where $\alpha = 2e\hbar v_F^2$ is a constant with e the electronic charge, \hbar Planck constant, and v_F Fermi velocity (Note S1, Supporting Information).^[23,24] For pristine graphene, each LL has a fourfold of double-spin and double-valley degeneracy.^[25,26] At each fixed Fermi energy E_F , the discrete set of N aligns linearly on a fan of lines $N = pm(E_F^2)/\alpha B \pm 1/2$, where $\pm 1/2$ comes from the zeroth LL, forming the so-called Landau-fan diagram. In pristine graphene, the slope β of this Landau-fan diagram is only determined by Fermi energy following (Note S2, Supporting Information):

$$\beta = \pm \frac{E_F^2}{\alpha} \quad (1)$$

The oscillation frequency B_F , derived from the magnitude of β , is thus also a function of Fermi energy. For pristine graphene, the linear extrapolation of carrier-density dependence of B_F for electrons and holes will cross B_F at zero at Dirac point (Figure 1a).

In proximity to a magnetic substrate, graphene's time-reversal symmetry can be broken, which can lift its spin-degeneracy (i.e., graphene is spin-polarized).^[11–13] As a consequence, LLs of spin-polarized graphene will be modified by a spin splitting term: $E_N^{(\uparrow,\downarrow)} = \text{sgn}(N^{(\uparrow,\downarrow)})\sqrt{\alpha B \times \sqrt{|N^{(\uparrow,\downarrow)}|} \pm \Delta/2}$, where $N^{(\uparrow,\downarrow)}$ is the index for spin-up and spin-down LLs and Δ is the spin splitting energy (Note S1, Supporting Information). For spin-polarized graphene, the energy spectrum will shift up and down by $\Delta/2$ for spin-up and spin-down LLs, respectively. Meanwhile, the slope β of the Landau-fan diagram will also be modified as (Note S2, Supporting Information):

$$\beta = \pm \left(\frac{2E_F^2}{\alpha} + \frac{\Delta^2}{2\alpha} \right) \quad (2)$$

Similar to the case of pristine graphene, the B_F of spin-polarized graphene is also a function of Fermi energy but with three distinct features: First, it depends on E_F and Δ that can be tuned independently. Second, it increases twice as fast ($\approx 2E_F^2/\alpha$), compared to that of pristine graphene ($\approx E_F^2/\alpha$). Third, the linear extrapolation of its carrier-density dependence for electrons and holes crosses B_F at a non-zero value of $\Delta^2/2\alpha$ at Dirac point (Figure 1b), in stark contrast to that of pristine graphene, which crosses at zero (Figure 1a). Therefore, we can use this non-zero intercept to evaluate the spin-splitting energy Δ in magnetic graphene.

2.2. Device Design and Characterization

As a proof of concept, we designed graphene/Tm₃Fe₅O₁₂ (G/TmIG) heterostructures, as shown in Figure 1c. TmIG was chosen to be the magnetic substrate for the following reasons: First, it is insulating so that graphene provides the only transport channel, making the tuning of Fermi energy possible.^[27] Second, it has a perpendicular magnetic anisotropy, and its orbital hybridizes with graphene sufficiently to induce a strong exchange coupling;^[28,29] and third, it has a low Gilbert damping and a high Curie temperature of 560 K, promising for a high-temperature magnetic exchange interaction.^[30] As a result, the

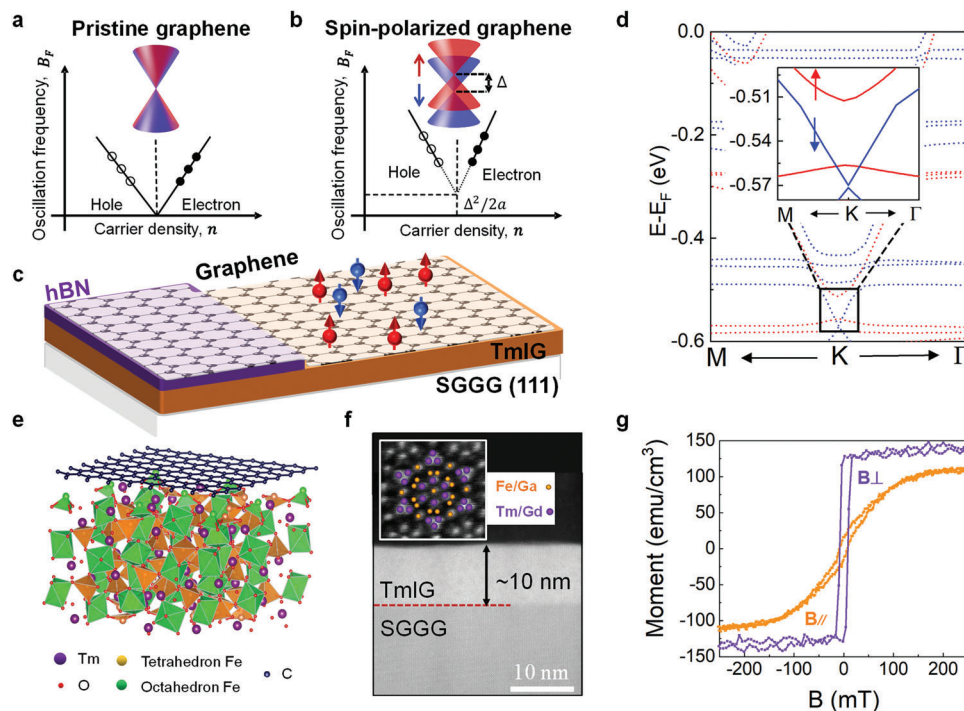


Figure 1. Characterizations and spin splitting in graphene (G) on $\text{Tm}_3\text{Fe}_5\text{O}_{12}$ (TmIG). Schematic of oscillation frequency B_F as a function of carrier density n a) for pristine graphene (The linear fits of electrons and holes extrapolate to zero-intercept at charge neutral point), and b) for spin-polarized graphene (In the region of $|E_F| > \Delta/2$, the linear fits of electrons and holes extrapolate to a non-zero intercept at charge neutral point). c) Schematic of G/TmIG heterostructure. The hBN is used to separate the graphene and TmIG as a contrast study. d) Calculated spin-resolved band structure of G/TmIG heterostructure. Bands in red (blue) correspond to spin up (down). The inset shows the enlargement of the calculated low energy bands at K point. e) Supercell for graphene on a $\text{Tm}_3\text{Fe}_5\text{O}_{12}$ (111) surface. Blue (the top layer), purple (large), yellow and green (medium), and red (small) colors represent C, Tm, Fe, and O atoms, respectively. f) Cross-sectional scanning tunneling electron microscopy (STEM) image for a TmIG/sGGG (111) sample viewed along the $[1\bar{1}0]$ direction. The red line marks the boundary between TmIG and sGGG. The inset shows the high-magnification plan-view STEM image with an overlay of the $[111]$ -projection of TmIG lattice. g) Magnetic hysteresis loops in perpendicular and in-plane magnetic fields of TmIG, showing the out-of-plane magnetic anisotropy.

unbalanced spin-up and spin-down electrons due to the lifting of the spin degeneracy will lead to spin-dependent quantum transport. Figure 1e shows a supercell used in the atomic and electronic structure calculation of graphene on a (111) surface of TmIG. There are two sites of Fe atoms in the TmIG unit cell: Fe^{3+} octahedral (Fe^{3+} Oh), two per formula unit and Fe^{3+} tetrahedral (Fe^{3+} Td), three per formula unit. The Fe^{3+} Td atoms are coupled antiferromagnetically to those Fe^{3+} Oh, but have a remanent magnetic moment.^[31] Figure 1d shows the optimized spin-polarized band structure of G/TmIG heterostructure. The Dirac cones are below the Fermi level and located inside the bandgap of TmIG. The inset zooms in the spin-polarized π bands near the Dirac point at K and shows that the induced spin splitting energy is ≈ 60 meV at an interlayer distance of 2.5 Å. Since the spin splitting is induced by the interaction between graphene and TmIG, the strength can be further enhanced by decreasing the separation between graphene and TmIG.^[12] For example, the spin splitting can be up to ≈ 133 meV at $d = 2.0$ Å under certain pressure, indicating a strong exchange interaction (Figure S1, Supporting Information).

High-quality TmIG thin films were epitaxially grown on (111)-oriented substituted gadolinium gallium garnet (SGGG) substrates by pulsed laser deposition (PLD) (see Experimental Section). Figure 1f shows a cross-sectional scanning tunneling elec-

tron microscopy (STEM) image of 10 nm TmIG coherently grown on SGGG without obvious dislocations with the red dashed line indicating TmIG/SGGG interface. The atomic arrangements of concentric hexagons are displayed in the high-magnification image, exhibiting a remarkable snowflake pattern (Inset of Figure 1f) (Figure S2, Supporting Information). Because of the negative magnetostriction constant of TmIG, the interfacial tensile strain exerted by SGGG produces a perpendicular magnetic anisotropy in TmIG.^[28,29] The magnetic hysteresis loops shown in Figure 1g confirm the out-of-plane magnetic anisotropy with an out-of-plane coercive field of a few oersteds and a saturation field of < 20 Oe, while the in-plane loop indicates a typical hard-axis behavior with a saturation field of ≈ 150 Oe. Our device structure is illustrated in Figure 2b. We place graphene on TmIG (also labeled as B-TmIG for clarity) using a PMMA/PMGI dry transfer technique (see Experimental Section).^[32] A top hBN (T-hBN) layer was then transferred to cover the entire graphene region, which simultaneously protects graphene from chemical contaminations and serves as a top-gate dielectric layer.^[33] At a section of the same sample, a 20-nm hBN buffer layer was inserted to screen the exchange interaction between graphene and TmIG as a contrast study (Figure S3, Supporting Information). Finally, a standard electron lithographic technique was used to create Hall bar geometry for electronic transport measurements.

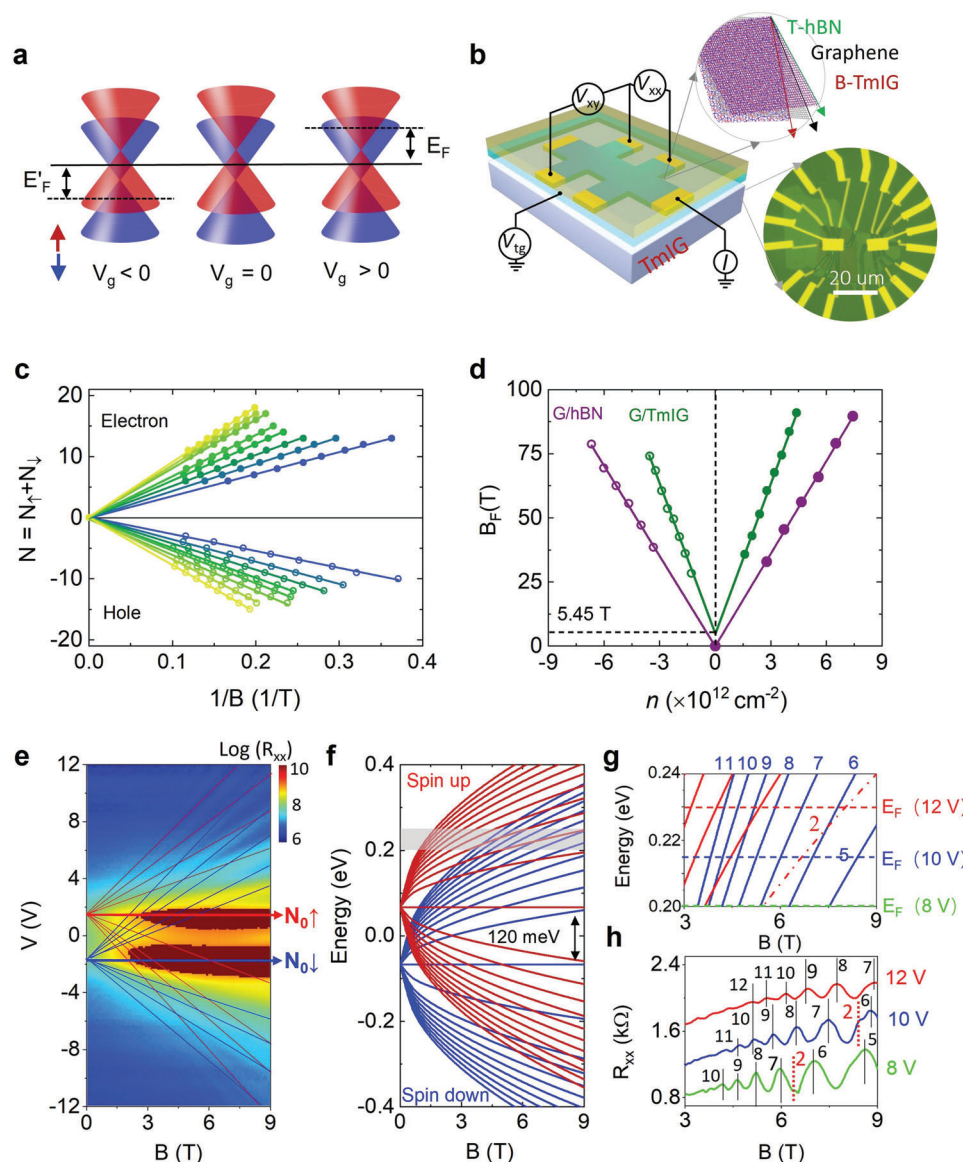


Figure 2. Quantum oscillations tuned by gate voltages in graphene on TmIG. a) Schematic of gate-tunable Fermi energy in spin-polarized graphene at a constant spin-splitting energy. The red and blue cones are the linear dispersion near the Dirac points corresponding to spin-up and spin-down electrons. b) Schematic of top-gate device and the art view of T-hBN/graphene/B-TmIG structure. The bottom right is the optical image of device. c) Landau-fan diagram of the Landau-levels (LLs) index N versus $1/B$ for gate voltages from ± 8 to ± 22 V (from blue to yellow). Each data point represents the value of $1/B$, where the N th minimum of R_{xx} occurs. The lines correspond to a linear fit with the slope indicating the B_F . d) The dependence of B_F on the carrier density n for G/TmIG and G/hBN. The positive n corresponds to electrons and negative to holes. e) A spin splitting Landau-fan diagram for G/TmIG. Longitudinal resistance R_{xx} versus magnetic field and gate voltage. f) Theoretical calculation of Landau-level spectrum with a given spin splitting energy. The split LL spectrum comprises up (red) and down (blue) spins. The position of E_F is denoted by the dark shadow area. g) Zooming-in LL states between 3 and 9 T and $E_F = 0.20$ – 0.24 eV from f. The red dashed line highlights the spin-up LL $N \uparrow = 2$. h) The measured Shubnikov-de Haas (SdH) oscillations at gate voltages of 8, 10, and 12 V. Data in panels c–d are from device D1; Panels e–h from device D2. $T = 2$ K.

We have studied several devices and focused on two of them (device D1 and D2) showing representative transport behavior.

2.3. Determination of Spin-Splitting Energy

First, we study gate-voltage tuning of SdH oscillations at a constant spin splitting energy of G/TmIG heterostructure

(Figure 2a). Similar to graphene on silicon dioxide,^[34] the electron and hole carriers in G/TmIG can also be tuned by gate voltages. The gate voltages tune the Fermi energy, leading to the modulation of oscillation frequency,^[25,26] as shown in Figure S4 (Supporting Information) for gate voltages from ± 8 to ± 22 V at 2 K. In order to obtain B_F , we extract LL indices by assigning consecutive integers to each SdH dip. Because $N \rightarrow 0$ has to be satisfied for $1/B \rightarrow 0$, there is only one way to assign the integer values of N to

the SdH dips (Figure S5, Supporting Information).^[20] Based on this, the sequence of values of $1/B_N$ is then plotted against N indices, showing a linear fan diagram (Figure 2c). The B_F can then be derived from the integer change in the slopes of this fan diagram, and the dependence of B_F on the carrier density n is shown in Figure 2d. For G/TmIG heterostructure, the electron and hole carriers both exhibit a linear dependence $B_F = c_1 n + b$, with $c_1 = 1.98 \times 10^{-15} \text{ Tm}^2$ ($\pm 2\%$) and $b = 5.45 \text{ T}$ ($\pm 6\%$), where \pm refers to the standard error for linear fitting. As can be seen in Figure 2d, a distinct feature is that while the linear extrapolation of B_F has a zero intercept at Dirac point for G/hBN heterostructure (Figure S6, Supporting Information), it is extrapolated toward a non-zero intercept ($B_F = 5.45 \text{ T}$) for the G/TmIG heterostructure, consistent with the model discussed in Figure 1a,b. Using the B_F intercept of 5.45 T, we can quantify Δ in device D1 to be 132 meV at 2 K, in good agreement with the theoretical calculation based on the split LL spectra (Figure S7, Supporting Information). Moreover, the Hall plateau value also provides further verification of the predicted LL structure with a given spin-splitting, calculated by appropriately summing the Chern numbers of the LLs from the spin-up and down sub-bands (Figure S8, Supporting Information).

Since each peak in the SdH oscillation corresponds to a crossing between one LL and Fermi level, we can examine the signature of spin splitting by comparing the measured color mapping of Landau-fan diagram to the splitting in the LL spectrum (Figure 2e–h). Another distinct feature can be seen in the color maps of the Landau-fan diagram. For G/hBN, there is a single conventional Landau-fan diagram, where the trajectory of each quantum oscillation evolves in a straight line away from the CNP at zero fields (Figure S9, Supporting Information). In stark contrast with G/hBN, G/TmIG shows a splitting Landau-fan diagram, where the entire sequence of spin-up and spin-down LL crossings can be seen in the map (Figure 2e). The Landau-fan diagram splits into two sets, sitting at the two sides of the zero-gate voltage. The split trajectory of each quantum oscillation evolves in a straight line away from the two sides. This feature is absent in the Landau-fan diagram of G/hBN since no spin splitting is involved. For the split Landau diagram, the LLs of graphene are modified by a spin-splitting term: $E_N^{(\uparrow,\downarrow)} = \text{sgn}(N^{(\uparrow,\downarrow)})\sqrt{\alpha B} \times \sqrt{(|N^{(\uparrow,\downarrow)}|) \pm \Delta/2}$, where $N^{(\uparrow,\downarrow)}$ is the index for spin-up and spin-down LLs and Δ is the spin-splitting energy, as drawn in Figure 2f. Compared with this theoretical Landau-fan spectrum, the two sets of Landau-energy levels are spin-up and spin-down diagram. At positive $V_{\text{TOP}} = +1.5 \text{ V}$, well-defined LLs are seen as part of a Landau fan from LLs with $N = 0, 1, 2, \dots$. At negative $V_{\text{TOP}} = -1.5 \text{ V}$, LLs emerge from a second Landau fan. The split two sets of the Landau-fan diagram sit at the two sides of the zero-gate voltage associated with the spin-up and spin-down spectrum. The observed splitting energy and the calculated LL fan diagram are consistent with the data in Figure 2e. Therefore, the full-color map of the Landau-fan diagram can visualize the spin splitting in G/TmIG. Second, by zooming-in the LL crossing between 3 and 9 T (Figure 2g), there is a spin-up LL $N\uparrow = 2$ (red dashed line) located between spin-down LL $N\downarrow = 6$ and $N\downarrow = 7$ at Fermi energy of 0.20 eV. With the increase of Fermi level, the spin-up LL $N\uparrow = 2$ will shift right and finally cross $N\downarrow = 6$ toward $N\downarrow = 5$. This physical picture is consistent with the measured SdH oscillations (Figure 2h). At a gate voltage of 8 V

($E_F = 0.20 \text{ eV}$), there is a shoulder peak belonging to $N\uparrow = 2$ located between $N\downarrow = 6$ and $N\downarrow = 7$. With the gate voltage increases to 10 V ($E_F = 0.215 \text{ eV}$), the shoulder peak shifts right and finally disappear at a gate voltage of 12 V ($E_F = 0.23 \text{ eV}$), consistent with the physical picture in Figure 2g. While for $N\uparrow = 3$, the LLs are dense and therefore cannot be distinguished by R_{xx} . Therefore, by using the combined split LL spectra and measured color map of the Landau-fan diagram, we can conclude that the spin splitting is induced in G/TmIG heterostructure that can be tuned by a gate voltage.

2.4. Cooling-Field Tuning of Spin-Splitting Energy

Next, we study the field-cooling tuning of the SdH oscillations at a constant Fermi energy in G/TmIG heterostructure (Figure 3a). By applying a magnetic field perpendicular to the sample plane during cooling (namely cooling field, B_{FC}), a remnant out-of-plane magnetic moment can be produced in the heterostructures. This field-cooling technique provides another knob that can be used to tune the splitting energy of spin-polarized G/TmIG heterostructures by flipping the applied magnetic field direction, where a positive cooling field results in an increase while a negative cooling field results in a decrease of the spin splitting energy,^[20] as illustrated in Figure 3a. Since the intercept of B_F is also directly related to the spin-splitting energy (Figure 1b), the modulation of this spin-splitting energy by field cooling can then be revealed from the intercept of B_F at Dirac point, B_0 (Figure 3b). For cooling field measurements, the samples were cooled down to 2 K starting from 350 K under an external magnetic field (see Experimental Section). Without a cooling field, the intercept B_0 is 5.45 T, corresponding to a spin splitting energy of 132 meV. By applying a negative cooling field of -9 T , the intercept B_0 decreases from 5.45 to 3.06 T, indicating that the spin splitting energy decreases from 132 to 98 meV. While using a positive cooling field of $+9 \text{ T}$, the intercept B_0 increases to 8.65 T, indicating that the spin splitting energy increases to 166 meV (Figure S10, Supporting Information). Therefore, a cooling field of up to 9 T can then be used to tune the spin splitting energy between 98 and 166 meV in G/TmIG (Inset of Figure 3b).

Figure 3c illustrates the energy shift of LLs by field cooling. By applying a positive cooling field, the increase of the spin splitting energy right-shifts the LL $N\downarrow = 6$, while for a negative cooling field, the decrease of the spin splitting energy shifts the LL $N\downarrow = 6$ to the opposite direction. In order to study the tunability of spin-splitting energy by field cooling, we set the Fermi energy at a constant of 0.19 eV by applying a top gate voltage $V_{\text{TOP}} = 12 \text{ V}$. The shift of the energy spectrum can then be observed using SdH oscillations. As can be seen from Figure 3d, at 12 V, the peak position of $N\downarrow = 6$ is $\approx 8.14 \text{ T}$ at zero cooling field. Applying a positive cooling field of $+9 \text{ T}$ right-shifts this peak to 8.61 T, while applying a negative cooling field of -9 T left-shifts the peak to 7.57 T, consistent with the physical picture in Figure 3c. On the other hand, no obvious shift was observed for G/hBN heterostructure, indicating that the exchange interaction between graphene and TmIG has been screened by hBN (Figure S11, Supporting Information). Moreover, the shifts in the Hall signal of G/TmIG are also consistent with the shifts in the SdH oscillations, i.e., the Hall plateau right-shifts with the positive cooling field and

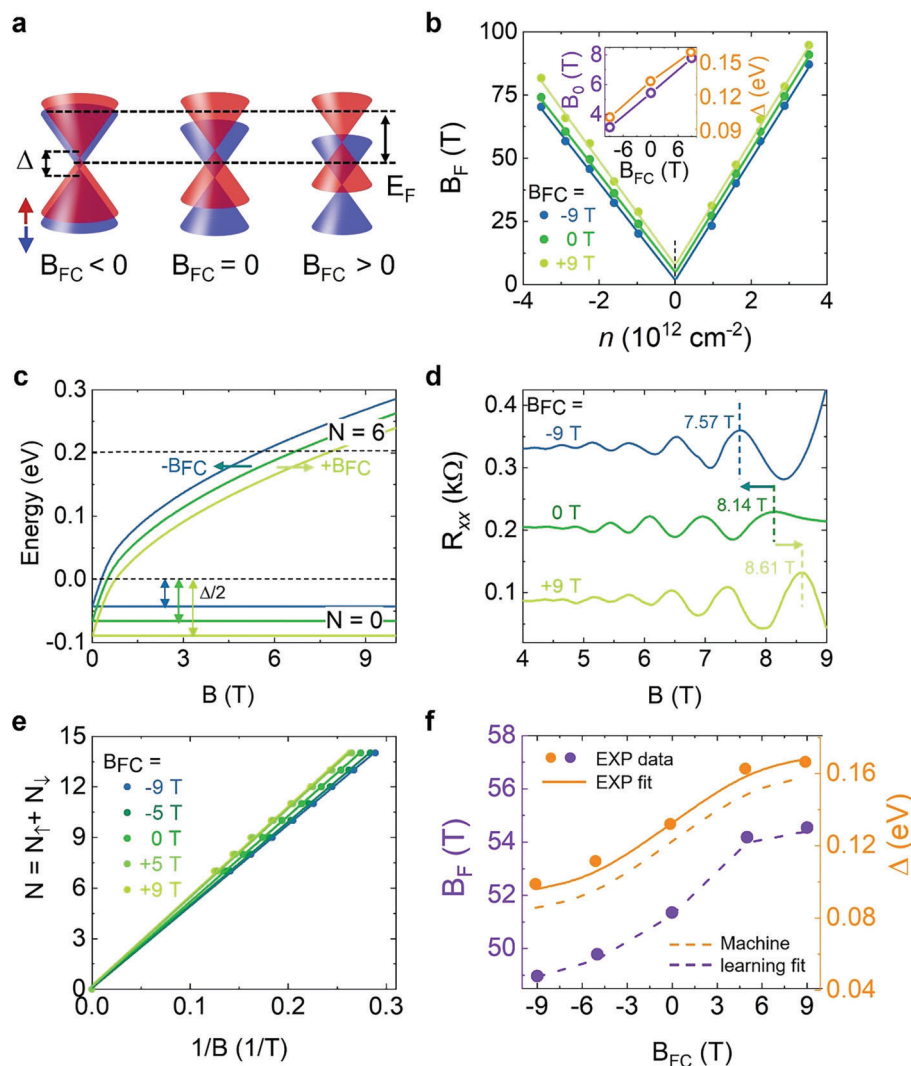


Figure 3. Quantum oscillations tuned by field cooling in graphene on TmIG. a) Schematic of spin-splitting energy tuned by field cooling in spin-polarized graphene at a constant Fermi energy. b) The dependence of B_F on the carrier density n at cooling fields of 0 and ± 9 T. The inset shows the dependence of intercept B_0 and the corresponding spin-splitting energy on the cooling fields. c) Illustration of spin-down Landau-levels (LLs) $N_{\downarrow} = 6$ shifted by field cooling. d) The shift of quantum oscillations by field cooling at the gate voltage of 12 V. The peaks of $N_{\downarrow} = 6$ are marked by the dashed lines. e) LLs indices N are extracted in the Landau-fan diagram for different cooling fields, showing a linear relationship. f) The oscillation frequency and the spin splitting energy tuned by field cooling. The solid dots and lines are experimental data, and the dashed lines are model fitting by a machine learning method. Data in panels b–f are from device D1. $T = 2$ K.

left-shifts with the negative cooling field (Figure S12, Supporting Information). These transport studies suggest that the band structure of graphene shifts with E_F because of the spin splitting, which can be tuned by the field cooling.

To further study the field-cooling dependence of B_F , we also plot R_{xx} as a function of $1/B$ for different cooling fields, from which discrete sets of LL-indices N linearly proportional to $1/B$ were obtained with slopes of β for different cooling fields (Figure 3e). According to the slopes of the Landau-fan diagram, the B_F tuned by cooling fields has a range of 48.6–54.3 T. Since the Fermi energy is 0.19 eV at 12 V, it can be deduced that the spin splitting energy under the field cooling of ± 9 T can be tuned between 98 and 166 meV (Figure 3f). To examine the induced spin-splitting energy in G/TmIG, we then used

a machine learning method to extract E_F and Δ by fitting the experimental data of B_F , which automatically generate the values of Fermi energy and spin splitting energy by minimizing the loss function (see Experimental Section). By solving a standard machine learning problem, these four parameters can be obtained: $E_F = 0.193$ eV, $\Delta_0 = 0.122$ eV, $\Delta_1 = 0.038$ eV, and $\lambda = 0.21$ T $^{-1}$ (Figure S13, Supporting Information). The machine learning fitting shows that in G/TmIG heterostructure, the Fermi energy is 0.193 eV at 12 V, which is quite close to our experimental data of 0.19 eV (0.2% error). Moreover, the spin splitting energy is 122 ± 36 meV (dashed lines in Figure 3f), where 122 meV is the spin splitting energy without field cooling, close to our experimental data of 132 meV (7.6% error). These results emphasize that spin splitting is indeed induced in graphene on

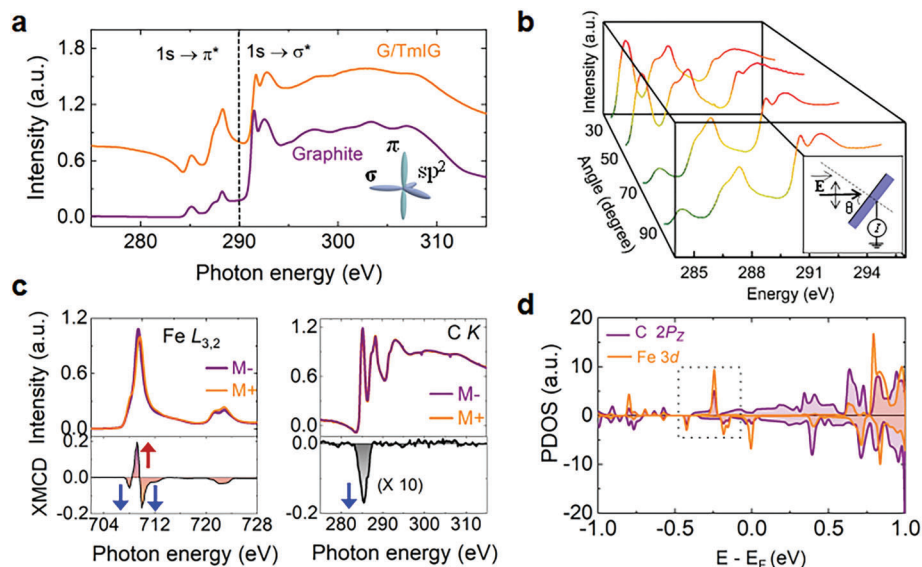


Figure 4. X-ray absorption spectroscopy (XAS) and X-ray magnetic circular dichroism (XMCD) of C K-edge and Fe L-edge. a) XAS acquired at the carbon K-edge of the G/TmIG. The inset shows the sp^2 hybrid orbitals: One s orbital and two p orbitals form a σ bond with trigonal planar structure. The half-filled P_z orbitals, perpendicular to the planar structure, form the π bonding and π^* antibonding band touching at the corner of the hexagonal Brillouin zone. b) Angle-dependent C K-edge spectra of the G/TmIG. The incident angle is the angle between the electrical vector of the light and the normal of the surface. c) XMCD spectra of the G/TmIG system: Absorption spectra of the Fe $L_{2,3}$ - and C K-edges are measured at $\pm 2T$ magnetic field. The corresponding XMCD signals are shown in the lower panels of the respective figures. d) The partial density of states (PDOSs) of Fe 3d orbitals and C $2P_z$ orbitals. The dashed square box highlights the overlaps of orbitals.

TmIG, and the field cooling can be used to tune the spin splitting energy.

2.5. XMCD Measurement of the Spin Polarization

Finally, in order to directly identify the origin of the proximity-induced magnetism in graphene by TmIG, we applied elemental-specific techniques, synchrotron radiation-based X-ray absorption spectroscopy (XAS) and XMCD.^[35] These measurements uniquely provide the origin of the magnetic momentum and coupling at the interface. The detailed sample structure and experimental configuration are shown in Figure S14 (Supporting Information). **Figure 4a** shows two pronounced regions 283–289 and 289–315 eV, which are ascribed to the transitions of core electrons into π^* ($C 1s \rightarrow \pi^*$) and σ^* orbitals ($C 1s \rightarrow \sigma^*$), respectively. Compared with pure graphite in the transitions of $C 1s \rightarrow \pi^*$ and $C 1s \rightarrow \sigma^*$, the spectra collected for G/TmIG become broadened and shifted to higher photon energy (≈ 0.1 eV), which can be attributed to the orbital hybridization at the interface between graphene and TmIG.^[36] **Figure 4b** further shows the angle-dependent XAS spectra at C K edge. The spectral feature around 285 eV, which is assigned to the transitions of $C 1s \rightarrow \pi^*$, is significantly enhanced when X-ray is at grazing incidence (30°) and vanishes for increasing incident angle, indicating that the π^* unoccupied states of $C 2P_z$ orbitals are aligned out-of-plane in the sp^2 coordination.

Figure 4c shows XMCD spectra of the G/TmIG system. The Fe $L_{3,2}$ XAS and XMCD spectrum, which shows positive and negative peaks corresponding to tetrahedral (Tet Fe^{3+}) and octahedral (Oct Fe^{3+}) sites, respectively, which have antiparallel cou-

pled spins.^[37] The most important finding is the observation of the obvious XMCD contrast at the C K absorption edge. The C K spectrum has the maximum asymmetry at 285 eV, indicating an induced magnetism in graphene, and also that the magnetism mainly comes from the spin-polarized $C 2P_z$ orbitals.^[35,36] Moreover, from the negative sign of the XMCD signal, we can conclude that the orbital moment of graphene is aligned parallel to the moment of the Oct Fe^{3+} , which is consistent with our first-principles calculations. As shown in **Figure 4d**, the partial density of state (PDOS) shows an overlap of Fe 3d and $C 2P_z$ orbitals, highlighted by the dashed square box, suggesting that the $C 2P_z$ orbitals of graphene are spin polarized due to the hybridization of the Fe 3d and the C-pz orbitals. Therefore, by combining XMCD and first-principles calculations, we can conclude that the hybridization between graphene π band and Fe 3d band leads to partial charge transfer from TmIG substrate to the spin-polarized electronic states of graphene, leading to the induced magnetism in graphene.

3. Conclusion

We have demonstrated that the insulating TmIG with perpendicular magnetic anisotropy can hybridize with graphene sufficiently to induce a strong spin-splitting energy. The present measurement concept based on Landau-fan shifts allows us to directly quantify the spin splitting energy, which is supported by our first-principles calculations and machine learning fitting. The combination of direct determination of spin-splitting energy and the theoretical calculations may also help reduce the discrepancies between theoretical predictions and experimental findings in other magnetic graphene heterostructures, for

example, graphene/ $Y_3Fe_5O_{12}$ heterostructure.^[14,16,21] However, we note that spin-splitting energy in magnetic graphene might not only be affected by the proximity strength between the two adjacent materials but also by interfacial quality such as roughness, defects, dangling bonds, and chemical contaminants (Figure S15, Supporting Information). This interface quality could also lead to the observed discrepancy between theoretical prediction and experimental findings. Therefore, the development of dry transfer in our work or direct large-scale growth of graphene on a magnetic substrate can ensure high-quality interface,^[8,15] maximizing the spin splitting energy in magnetic graphene, and finally leading to substantial advances in 2D spintronics with a long-distance transfer of spin information and ultrafast operation.

4. Experimental Section

Growth and Characterization of TmIG Film: The high-quality TmIG thin films were grown by pulsed laser deposition on (111)-oriented SGGG substrates (lattice constant $a = 12.56 \text{ \AA}$) to achieve high tensile strain ($\approx 2\%$). Due to its negative magnetostriction constant, a large perpendicular magnetic anisotropy would be induced in TmIG. The base pressure of the deposition chamber was $\approx 5 \times 10^{-7}$ Torr. The TmIG films were grown at a temperature of $650 \text{ }^\circ\text{C}$ by KrF excimer laser pulses of 248 nm in wavelength with a power of 85 mJ at a repetition of 10 Hz under 200 mTorr oxygen pressure. Atomic force microscopy (AFM) root mean square (RMS) roughness measurements were carried out in a digital instruments nanoscope IV with a $1 \times 1 \text{ }\mu\text{m}$ scan size. Tapping-mode AFM of the 10-nm -thick TmIG sample used in this study gave an RMS roughness of $\approx 0.13 \text{ nm}$. The cross-section and plane-view TEM sample were prepared by using a focused ion beam (FIB) at 30 kV (FEI, Helios G4 UX), followed by a low-voltage ion beam cleaning process at 5 kV to minimize the surface amorphization of the TEM lamella. High-angle annular dark-field STEM was performed by FEI Titan 60/300 STEM operated at 300 kV with a probe corrector. A SQUID magnetometry has been used to measure the magnetic moment of the TmIG/SGGG system in out-of-plane and in-plane magnetic field configuration at room temperature. The hysteresis loops of the magnetizations in both cases are measured by sweeping the applied magnetic field from positive to negative and back again to positive. Thereafter, we subtract the linear background of the paramagnetic SGGG substrate from the raw data and obtain the magnetic anisotropy of TmIG.

Device Fabrication: To fabricate a G/TmIG device, natural graphite (NGS, Germany) was first mechanically exfoliated on a PMGI/PMMA-coated silicon substrate. After identifying the single-layer graphene by Raman spectroscopy, the PMGI layer was slowly dissolved by the MF319 solution, and subsequently, the graphene/PMMA bilayer was cleaned thoroughly in DI water. The graphene/PMMA bilayer was then transferred onto the TmIG using the dry-transfer technique. Finally, the PMMA layer was removed by acetone, and the single-layer graphene on TmIG was finally obtained. To fabricate a top gate device, the graphene was firstly etched into a standard Hall bar structure on TmIG, then annealed at $350 \text{ }^\circ\text{C}$ for 2 h under H_2/Ar gas to remove the PMMA residue. After this, a top hBN layer with $20\text{--}30 \text{ nm}$ was transferred to cover the entire graphene region, which simultaneously protects graphene from chemical contaminations and serves as a top-gate dielectric layer. Finally, the Cr/Au electrodes were deposited on the top hBN.

Magneto-Transport Measurement: The electrical transport measurements were carried out in a physical property measurement system (PPMS) interfaced with source meters (Model 2400, Keithley Inc.) and multimeters (Model 2002, Keithley Inc.). A direct current of $1 \text{ }\mu\text{A}$ was applied through the sample to measure the longitudinal resistance and Hall resistance in a magnetic field (perpendicular to the sample plane) with the magnitude varying from -9 to 9 T . To apply top-gate bias, the source terminal was connected to the top-gate electrode, and the leakage current

through the top hBN layer was monitored. This work used the Hall measurement to directly extract the carrier density. This work first measured the R_{xy} change with top gate voltage under a low magnetic field of $B = 1 \text{ T}$. After that, the Hall charge carrier density, $n = B/R_{xy} e$, was used to get the relationship between carrier density and top gate voltage. For cooling field measurements, the samples were cooled down to 2 K starting from 350 K (staying there for $\approx 600 \text{ s}$), and the longitudinal and transverse Hall effect was measured simultaneously from $\pm 9 \text{ T}$ magnetic fields.

X-Ray Magnetic Circular Dichroism: The X-ray absorption and the XMCD measurements were carried out at the SINS beamline of the Singapore Synchrotron Light Source (SSLS). The base pressure during measurements was $\approx 1 \times 10^{-10}$ mTorr. The X-ray beam was focused to about $2 \times 0.2 \text{ mm}$, and a gold mesh was used for incident flux signal normalization. The X-ray absorption signal was measured with a Keithley 9527 current amplifier via the sample-to-ground drain current (total electron yield TEY signal). All measurements were conducted in a magnetic field of 2 T generated collinearly with the incoming X-ray direction by a superconducting vector-cryomagnet (Scientific Magnetics). This field strength was chosen to align the net magnetization without causing a spin-flip. The XMCD was taken as the difference of the XAS spectra, i.e., $M^- - M^+$, obtained by flipping the X-ray at a fixed magnetic field of 2 T , under which the sample was fully magnetized.

Theoretical Calculations: The first-principles calculations were performed by using the projected augmented-wave method as implemented in the Vienna ab initio simulation package (VASP). The generalized gradient approximation (GGA) of the Perdew–Burke–Ernzerhof type was utilized to treat the exchange–correlation interaction. In the calculations, a 7×7 graphene supercell was used to match the 1×1 TmIG (111) substrate, with a lattice mismatch of about 2.2% . The dangling bond of the TmIG (111) substrate on the bottom surface was passivated with hydrogen atoms. A vacuum buffer layer of 20 \AA was set to avoid interaction between adjacent layers. During structural optimization, the atoms of graphene and TmIG (111) from the top three atomic layers were allowed to relax. The Hellmann–Feynman force tolerance criterion, kinetic energy cutoff, and energy convergence threshold were set to be 0.01 eV \AA^{-1} , 520 eV and 10^{-4} eV , respectively. A Γ -centered $3 \times 3 \times 1$ k-mesh was adopted. The $3d$ states of Fe were treated with the GGA+ U approach, with $U_{\text{eff}} = 2.7 \text{ eV}$.

For machine learning fitting, one approximation was made: Under high field cooling, the splitting energy would saturate at high cooling fields, and thus the magnitude of splitting energy was assumed to be the tanh function of B_{FC} :

$$\Delta(B_{FC}) = \Delta_0 + \Delta_1 \tanh(\lambda B_{FC}) \quad (3)$$

where Δ_0 is the splitting energy at zero cooling field, Δ_1 denotes the magnitude of the modulation by field cooling, and λ is the fitting parameter in the tanh function. Combining Equations (2) and (3) results in four parameters $X = [E_F, \Delta_0, \Delta_1, \lambda]$. The conjugate gradient method was then utilized to determine the model parameters of $X = (\epsilon_F, \Delta_0, \Delta_1, \xi)^T$. The procedure can be summarized as follows: (i) define loss function as $\phi(X) = \sum_i [\beta(B_{FC}^i, X) - \hat{\beta}(B_{FC}^i)]^2 / \sum_i \hat{\beta}^2(B_{FC}^i)$, where $\beta(B_{FC}^i, X)$ and $\hat{\beta}(B_{FC}^i)$ represent predicted and experimental Landau-fan slopes, respectively. (ii) Minimize the loss function $\phi(X)$ using a nonlinear conjugate gradient algorithm. (iii) Obtain the optimized $X_0 = \text{argmin} \phi(X)$. The fitting algorithm eventually obtained a stable local minimal of $\phi(X)$ that was smaller than 2×10^{-5} . As displayed in Figure S9 (Supporting Information), the variation of the initial value of X does not change the converged value of X_0 , indicating the stability and accuracy of the fitting algorithm.

Supporting Information

Supporting Information is available from the Wiley Online Library or from the author.

Acknowledgements

J.X.H., Y.L.H., and X.C. contributed equally to this work. This work was supported by the Ministry of Education (MOE) Singapore under the Academic Research Fund Tier 2 (Grant No. MOE-T2EP50120-0015), by the Agency for Science, Technology and Research (A*STAR) under its Advanced Manufacturing and Engineering (AME) Individual Research Grant (IRG) (Grant No. A2083c0054), and by the National Research Foundation (NRF) of Singapore under its NRF-ISF joint program (Grant No. NRF2020-NRF-ISF004-3518). The work at USTC was financially supported by the National Natural Science Foundation of China (Grant Nos. 11974327 and 12004369), Fundamental Research Funds for the Central Universities (Grant Nos. WK3510000010 and WK2030020032), Anhui Initiative in Quantum Information Technologies (Grant No. AHY170000) and Innovation Program for Quantum Science and Technology (Grant No. 2021ZD0302800). The authors also thank the supercomputing service of AM-HPC and the Supercomputing Center of the USTC for providing the high-performance computing resources. K.W. and T.T. acknowledge support from the Elemental Strategy Initiative conducted by the MEXT, Japan (Grant Number JPMXP0112101001) and JSPS KAKENHI (Grant Numbers 19H05790, 20H00354, and 21H05233).

Conflict of Interest

The authors declare no conflict of interest.

Data Availability Statement

The data that support the findings of this study are available from the corresponding author upon reasonable request.

Keywords

2D materials, complex oxides, field cooling, Landau-fan diagram, spin-polarization

Received: June 15, 2023

Revised: October 1, 2023

Published online:

- [1] J. F. Sierra, J. Fabian, R. K. Kawakami, S. Roche, S. O. Valenzuela, *Nat. Nanotechnol.* **2021**, *16*, 856.
- [2] X. Lin, W. Yang, K. L. Wang, W. Zhao, W. S. Zhao, *Nat. Electron.* **2019**, *2*, 274.
- [3] B. Huang, M. A. McGuire, A. F. May, D. Xiao, P. Jarillo-Herrero, X. Xu, X. D. Xu, *Nat. Mater.* **2020**, *19*, 1276.
- [4] T. S. Ghiasi, A. A. Kaverzin, A. H. Dismukes, D. K. De Wal, X. Roy, B. J. Van Wees, *Nat. Nanotechnol.* **2021**, *16*, 788.
- [5] B. Behin-Aein, D. Datta, S. Salahuddin, S. Datta, *Nat. Nanotechnol.* **2021**, *5*, 266.
- [6] N. Tombros, C. Jozsa, M. Popinciuc, H. T. Jonkman, B. J. Van Wees, *Nature* **2007**, *448*, 571.
- [7] W. Han, R. K. Kawakami, M. Gmitra, J. Fabian, *Nat. Nanotechnol.* **2014**, *9*, 794.
- [8] P. Wei, S. Lee, F. Lemaitre, L. Pinel, D. Cutaia, W. Cha, F. Katmis, Y. Zhu, D. Heiman, J. Hone, J. S. Moodera, C.-T. Chen, *Nat. Mater.* **2016**, *15*, 711.
- [9] S. Singh, J. Katoch, T. Zhu, K.-Y. Meng, T. Liu, J. T. Brangham, F. Yang, M. E. Flatté, R. K. Kawakami, *Phys. Rev. Lett.* **2017**, *118*, 187201.
- [10] C. L. Tang, Z. W. Zhang, S. Lai, Q. H. Tan, W. B. Gao, *Adv. Mater.* **2022**, *32*, 1908498.
- [11] H. X. Yang, A. Hallal, D. Terrade, X. Waintal, S. Roche, M. Chshiev, *Phys. Rev. Lett.* **2013**, *110*, 046603.
- [12] Z. Qiao, W. Ren, H. Chen, L. Bellaiche, Z. Zhang, A. H. Macdonald, Q. Niu, Q. Niu, *Phys. Rev. Lett.* **2014**, *112*, 116404.
- [13] P. Högl, T. Frank, K. Zollner, D. Kochan, M. Gmitra, J. Fabian, *Phys. Rev. Lett.* **2020**, *124*, 136403.
- [14] Z. Wang, C. Tang, R. Sachs, Y. Barlas, J. Shi, *Phys. Rev. Lett.* **2015**, *114*, 016603.
- [15] D. V. Averyanov, I. S. Sokolov, A. M. Tokmachev, O. E. Parfenov, I. A. Karateev, A. N. Taldenkov, V. G. Storchak, *ACS Appl. Mater. Interfaces* **2018**, *10*, 20767.
- [16] J. C. Leutenantsmeyer, A. A. Kaverzin, M. Wojtaszek, B. J. van Wees, *2D Mater.* **2017**, *4*, 014001.
- [17] J. Ding, Z. Qiao, W. Feng, Y. Yao, Q. Niu, *Phys. Rev. B* **2011**, *84*, 195444.
- [18] H. Zhang, C. Lazo, S. Blügel, S. Heinze, Y. Mokrousov, *Phys. Rev. Lett.* **2012**, *108*, 056802.
- [19] M. Jugovac, I. Cojocariu, J. Sánchez-Barriga, P. Gargiani, M. Valvidares, V. Feyer, S. Blügel, G. Bihlmayer, P. Perna, *Adv. Mater.* **2023**, *35*, 2301441.
- [20] Y. Wu, G. Yin, L. Pan, A. J. Grutter, Q. Pan, A. Lee, D. A. Gilbert, J. A. Borchers, W. Ratcliff, A. Li, X.-D. Han, K. L. Wang, *Nat. Electron.* **2020**, *3*, 604.
- [21] A. Hallal, F. Ibrahim, H. Yang, S. Roche, M. Chshiev, *2D Mater.* **2017**, *4*, 025074.
- [22] A. H. Castro Neto, F. Guinea, N. M. R. Peres, K. S. Novoselov, A. K. Geim, *Rev. Mod. Phys.* **2009**, *81*, 109.
- [23] G. Li, E. Y. Andrei, *Nat. Phys.* **2007**, *3*, 623.
- [24] D. L. Miller, K. D. Kubista, G. M. Rutter, M. Ruan, W. A. De Heer, P. N. First, J. A. Stroscio, *Science* **2009**, *324*, 924.
- [25] K. S. Novoselov, A. K. Geim, S. V. Morozov, D. Jiang, M. I. Katsnelson, I. V. Grigorieva, S. V. Dubonos, A. A. Firsov, *Nature* **2005**, *438*, 197.
- [26] Y. Zhang, Y.-W. Tan, H. L. Stormer, P. Kim, *Nature* **2005**, *438*, 201.
- [27] C. O. Avci, A. Quindeau, C.-F. Pai, M. Mann, L. Caretta, A. S. Tang, M. C. Onbasli, C. A. Ross, G. S. D. Beach, *Nat. Mater.* **2017**, *16*, 309.
- [28] Q. Shao, Y. Liu, G. Yu, S. K. Kim, X. Che, C. Tang, Q. L. He, Y. Tserkovnyak, J. Shi, K. L. Wang, *Nat. Electron.* **2019**, *2*, 182.
- [29] S. Vélez, J. Schaab, M. S. Wörnle, M. Müller, E. Gradauskaite, P. Welter, C. Gutsell, C. Nistor, C. L. Degen, M. Trassin, M. Fiebig, P. Gambardella, *Nat. Commun.* **2019**, *10*, 4750.
- [30] C. Tang, C.-Z. Chang, G. Zhao, Y. Liu, Z. Jiang, C.-X. Liu, M. R. McCartney, D. J. Smith, T. Chen, J. S. Moodera, J. Shi, *Sci. Adv.* **2017**, *3*, e1700307.
- [31] A. Quindeau, C. O. Avci, W. Liu, C. Sun, M. Mann, A. S. Tang, M. C. Onbasli, D. Bono, P. M. Voyles, Y. Xu, J. Robinson, G. S. D. Beach, C. A. Ross, *Adv. Electron. Mater.* **2017**, *3*, 1600376.
- [32] J. X. Hu, J. Gou, M. Yang, G. Ji Omar, J. Y. Tan, S. W. Zeng, Y. P. Liu, K. Han, Z. S. Lim, Z. Huang, A. T. Shen Wee, A. Ariando, *Adv. Mater.* **2020**, *32*, 2002201.
- [33] J. Hu, J. Tan, M. M. Al Ezzi, U. Chattopadhyay, J. Gou, Y. Zheng, Z. Wang, J. Chen, R. Thottathil, J. Luo, K. Watanabe, T. Taniguchi, A. T. S. Wee, S. Adam, A. Ariando, *Nat. Commun.* **2023**, *14*, 4142.
- [34] K. S. Novoselov, A. K. Geim, S. V. Morozov, D. Jiang, Y. Zhang, S. V. Dubonos, I. V. Grigorieva, A. A. Firsov, *Science* **2004**, *306*, 666.
- [35] J. B. S. Mendes, O. Alves Santos, T. Chagas, R. Magalhães-Paniago, T. J. A. Mori, J. Holanda, L. M. Meireles, R. G. Lacerda, A. Azevedo, S. M. Rezende, *Phys. Rev. B* **2019**, *99*, 214446.
- [36] Y. S. Dedkov, M. Sicot, M. Fonin, *J. Appl. Phys.* **2010**, *107*, 09E121.
- [37] W. Liu, L. He, Y. Xu, K. Murata, M. C. Onbasli, M. Lang, N. J. Maltby, S. Li, X. Wang, C. A. Ross, P. Bencok, G. Van Der Laan, R. Zhang, K. L. Wang, *Nano Lett.* **2015**, *15*, 764.